Measuring serotonin binding to its receptors via charge transfer to ANAP

Olivia G. Brado[1], Aspen T. Hawkins[1], Adam D. Hill[1], and Michael C. Puljung[1,2]

[1]Department of Chemistry and [2]Neuroscience Program

Trinity College, Hartford, CT, USA

Keywords: serotonin, dopamine, fluorescence, ion channel, receptor

Abstract

Serotonin (5-HT) is a vital intercellular messenger with diverse signaling functions throughout the human body. We have characterized and implemented a novel, fluorescence-based method of measuring 5-HT binding to gain a fuller understanding of the interactions between 5-HT and its receptors. This method involves expression of 5-HT receptor proteins with the fluorescent, non-canonical amino acid L-3-(6-acetylnaphthalen-2-ylamino)-2-aminopropanoic acid (ANAP) incorporated into the ligand binding site. ANAP fluorescence was quenched in solution by both 5-HT and dopamine. Time-resolved photoluminescence and transient absorption spectroscopy confirmed that ANAP quenching by 5-HT involved a rapidly reversible charge-transfer process. Based on density functional theory calculations, this process likely involved a ANAP reduction by 5-HT as assessed using whole-cell patch clamp. To test this method on intact receptors in a cellular context, we expressed 5-HT_{3A} receptors (5-HT-gated ion channels) in HEK293T cells with ANAP inserted co-translationally into the transmitter binding site. Fluorescently labeled 5-HT_{3A} receptors were functional and activated by 5-HT. Addition of 5-HT caused a concentration-dependent quenching of fluorescence from ANAP-tagged channels expressed in intact cells and unroofed plasma membranes, demonstrating the utility of this method for measuring 5-HT binding to its receptors. Collectively, these results delineate a technique for measuring transmitter binding that can be widely adopted to measure 5-HT binding not only to 5-HT_3 receptors, but to any 5-HT receptor, transporter, or binding protein.

26 **Introduction.**

27 Serotonin (5-hydroxytryptamine, 5-HT) is a near-ubiquitous intercellular messenger, playing
28 crucial roles in blood, the gut, and the central nervous system (CNS) (Hensler, 2012). In the
29 CNS, 5-HT is primarily produced in the raphe nuclei of the brainstem, which project widely
30 throughout the brain and spinal cord. Through these projections, 5-HT modulates many diverse
31 neurobiological phenomena including arousal, mood, and pain transmission (Ossipov et al.,
32 2010; Kandel et al., 2021). Serotonergic dysfunction has been linked to numerous disease
33 states including major depressive disorder, drug use disorder, and inflammatory bowel disease.
34 Though a rich appreciation for 5-HT signaling and its interaction with its receptors is crucial to
35 gain a better understanding of its role in health and disease, existing methods for measuring 5-
36 HT binding fall short of providing direct, real-time information about receptor occupancy. In this
37 work, we propose, fully characterize, and employ a novel fluorescence-based method that
38 directly reports the binding of 5-HT its receptors in real time.

39 5-HT binds to a diverse group of receptor molecules. In humans, 5-HT receptors are grouped
40 into seven families (5-HT_1 through 5-HT_7), based on sequence homology (Hensler, 2012). Each
41 family encompasses several receptor subtypes. With the exception of the 5-HT_3 family of
42 receptors, all 5-HT receptors are G-protein coupled; binding of 5-HT prompts dissociation of
43 heterotrimeric G-proteins from its receptors triggering downstream, intracellular signaling
44 events. In contrast, 5-HT_3 receptors (5-HT_{3A}-5-HT_{3E} in humans) are part of the pentameric
45 ligand-gated ion channel (PLGIC) superfamily (Maricq et al., 1991; Gibbs and Chakrapani,
46 2021). Binding of 5-HT opens an aqueous pathway for cation flow across the plasma
47 membrane, generating an excitatory current. 5-HT_3 receptors are important regulators of brain-
48 gut signaling and the vomiting response and have been implicated in several disease processes
49 including inflammatory bowel disease (IBS), schizophrenia, and substance use disorder
50 (Engleman et al., 2008; Ellenbroek and Prinssen, 2015; Vahora et al., 2020).

To gain a richer understanding of structure-activity relationships in 5-HT receptors, we sought to develop an assay that would allow for real-time measurement of transmitter binding. Equilibrium binding assays operate over long time scales and non-physiological conditions. Biochemical assays of 5-HT binding depend on downstream signaling events and do not measure binding directly. Even measuring current evoked in voltage-clamp experiments on 5-HT_3 receptors provides only indirect information regarding ligand binding, as the binding equilibrium is directly coupled to the gating process.

An ideal ligand binding assay would meet five criteria: 1) it would allow for the measurement of 5-HT binding in real time, 2) be non-destructive and chemically reversible, 3) permit measurements to be made on intact, functional channels in living cells, 4) have a short distance dependance so binding can be measured site-specifically, and 5) be compatible with high-throughput biochemical assays and (for 5-HT_3 receptors) voltage clamp. In previous work, we developed such an assay to measure nucleotide binding to ATP-sensitive K^+ channels (K_{ATP})(Puljung et al., 2019; Usher et al., 2020b). This assay involved expression of channels labeled with the fluorescent, non-canonical amino acid L-3-(6-acetylnaphthalen-2-ylamino)-2-aminopropanoic acid (ANAP, Fig. 1A) (Chatterjee et al., 2013). ANAP can be introduced site-specifically into any site on a protein using amber stop-codon suppression. We previously used Förster resonance energy transfer (FRET) between ANAP and fluorescent ATP derivatives to measure binding to K_{ATP} (Puljung et al., 2019; Usher et al., 2020b). The strong distance-dependence of FRET allowed us to measure binding in a site-specific fashion (i.e. we were able to discriminate binding between three different classes on nucleotide-binding site on K_{ATP}).

We now report a method that allows measurement of 5-HT binding to its receptors and that satisfies the five criteria stated above. Reasoning that Prodan (structurally analogous to the side chain of ANAP) fluorescence is quenched by tryptophan and that 5-HT is derived from tryptophan, we first demonstrate that 5-HT, as well as dopamine (DA), quench ANAP in solution.

We further investigate this process using density functional theory, time-resolved photoluminescence and transient absorption spectroscopies to demonstrate that quenching occurs via a short-range electron transfer process that reversibly reduces ANAP. Finally, we expressed ANAP-labeled 5-HT_{3A} receptors in HEK293T cells and used this quenching to measure 5-HT binding to channels in the plasma membrane of living cells. These results point to the broad applicability of ANAP for directly interrogating the binding of 5-HT and dopamine to relevant receptors, allowing for an expanded understanding of their physiological signaling roles, as well as how dysfunction in that signaling produces pathological states.

Materials and methods.

UV/Vis absorbance and steady-state fluorometry. Stock solutions of ANAP (ASIS ChemInc., Waltham MA) were prepared at 20 mM in DMSO and diluted into DMSO or water. 5-HT and DA stocks were prepared at 200 mM in water or DMSO. Stocks were stored frozen at -20 °C. To reduce the impact of oxidation, all 5-HT and DA solutions were prepared fresh the day before experiments and kept frozen until the time of measurement. The absorbance of each ANAP/5-HT or ANAP/DA solution was measured using a Red Tide UBS650U spectrometer (Ocean Optics; Orlando, FL) and LoggerPro software (Vernier; Beaverton, OR). 5-HT and DA blank solutions were measured separately. All spectra were acquired using a low-volume quartz cuvette (Azzota Corp.; Claymont, DE).

The fluorescence emission spectrum of 20 μM ANAP in water or DMSO was measured in different concentrations of 5-HT or DA, as indicated. Spectra were acquired using a Hitachi F-7000 fluorescence spectrophotometer and FL Solutions software. The samples were excited at 370 nm and emission was measured between 380 nm and 600 nm. Slit widths were 5 nm on the excitation and emission side and the PMT was set to 700 V. Spectra were blank subtracted using emission spectra of 5-HT/DA solutions without ANAP. DA contributed very little to the fluorescence background, whereas 5-HT accounted for 15.2% of the total fluorescence signal at the peak wavelength for ANAP fluorescence (448 nm) measured for 20 μM ANAP plus 100 mM 5-HT in DMSO.

Emission spectra were corrected for the inner-filter effect (as indicated) using absorbance values measured as above and the following equation

$$F = F_{obs} * 10^{\frac{(0.2*OD_{ex}+OD_{em})}{2}}.$$

F_{obs} is the measured emission, OD_{ex} is the optical density at the excitation wavelength (370 nm) and OD_{em} is the optical density at each emission wavelength. The 0.2 term corrects for the low-volume cuvette, which had a short, 0.2 cm path oriented toward the excitation light. Before correction, UV/Vis spectra were smoothed in JMP (JMP Statistical Discovery LLC, Cary, NC) using local kernel smoothing with a local bandwidth of 0.25 nm.

Stern-Volmer plots were fit with a linear equation of the form

$$\frac{F}{F_0} = F_{intercept} + K_{sv} * [quencher],$$

where F is the averaged peak fluorescence between 445 nm and 455 nm for each solution, F_0 is the average fluorescence in the absence of quencher, and K_{sv} is the Stern-Volmer constant, reflecting the quenching efficiency. $F_{intercept}$ was the value extrapolated from the linear fit to zero [quencher]. This value is expected to be one and was found to be close to one in our fits.

Density functional theory calculations. The relative stability of fluorophore/quencher electron transfer pairs were computed using density functional theory (DFT). Q-Chem 5.2 was used to computer neutral singlet structures, as well as reduced and oxidized doublet structures, of each compound using the ωB97XD density functional and aug-cc-pVDZ basis set and a polarizable continuum model (ε = 80) (Chai and Head-Gordon, 2008; Shao et al., 2015). Doublet calculations were restricted to prevent spin contamination (Bursch et al., 2022). Following initial structure optimizations, harmonic frequency analysis confirmed that each structure represented a true local minimum (no imaginary frequencies) and provided values to determine ΔH and ΔS corrections at 310 K for the calculation of theoretical ΔG values (Tartakoff et al., 2021). Thermodynamics comparisons and plotting were performed using Python 3.9.13 with numpy 1.26.2 and matplotlib 3.8.0.

129 *Time-resolved spectroscopies.* Time-resolved photoluminescence (TRPL) and transient
130 absorption spectroscopy (TAS) measurements were performed using an Edinburgh Instruments
131 LP980 with a Litron Nano 5 Hz pump laser tripled to produce 355 nm, 8 ns pulses (FWHM).
132 Both TRPL and TAS data were taken with the LP980's PMT detector configured in its highest
133 time-resolution mode, corresponding to 400 ps time bins. TRPL measurements were performed
134 with the laser attenuator set to 10 mJ/pulse on solutions of 100 nM ANAP or 1.0 mM 5-HT in
135 DMSO; emission was measured at 480 nm for 64 averages. For TAS measurements, laser
136 power was lowered to 1 mJ/pulse and concentrations were increased to 1.0 mM ANAP and 10
137 mM 5-HT and were followed via ANAP radical anion peak at 440 nm for 500 averages (made
138 possible by the complete recovery of signals between shots.) Data were fit to a convolution of
139 the instrument response function (IRF; measurement of elastically scattered laser pulse after
140 passing through ND = 3 filter) and exponential decay function(s) using Edinburgh Instruments'
141 L900 software (Kolber and Barkley, 1986). Additional analysis and plotting were performed
142 using Python (see above).

143 *Molecular cloning.* Mouse 5-HT_{3A} in pICherryNeo was a gift from Dr. Sudha Chakrapani.
144 pCGFP_EU was a gift from Dr. Eric Gouaux (Kawate and Gouaux, 2006). mOrange-N1 was a
145 gift from Michael Davidson (Addgene plasmid # 54499 ; http://n2t.net/addgene:54499 ;
146 RRID:Addgene_54499) (Kremers et al., 2009). pANAP was a gift from Peter Schultz (Addgene
147 plasmid # 48696 ; http://n2t.net/addgene:48696 ; RRID:Addgene_48696) (Chatterjee et al.,
148 2013).

149 As a preliminary step, the GFP insert from pCGFP_EU was cloned into the 5-HT_{3A} sequence
150 in pICherryNeo at a position between amino acids D382 and S384 in the putatively unstructured
151 loop between transmembrane domains 3 and 4 (Basak et al., 2018). We used PCR
152 (QuickChange Kit; Agilent Technologies; Santa Clara, CA) to introduce new restriction sites into
153 the 5-HT_{3A} sequence and inserted the GFP tag using standard subcloning techniques. We

154 subsequently replaced this GFP tag with mOrange because the emission peak for mOrange
155 was farther from the expected ANAP peak. Stop-codon mutations were introduced using
156 QuickChange. All constructs were verified by direct sequencing at Azenta GeneWiz (South
157 Plainfield, NJ).

158 *Cell culture.* HEK-293T cells were purchased from ATCC (Manassas, VA). Frozen stocks were
159 prepared during early passages and stored in liquid nitrogen. Cells were verified by ATCC. We
160 performed no additional verification or mycoplasma testing. Cells were grown in T-75 flasks
161 (Grenier Bio-One; Monroe, NC) in Dulbecco's Modified Eagle Medium (DMEM; Gibco; Grand
162 Island, NY) supplemented with 10% fetal bovine serum (FBS; Corning; Tewksbury, MA), 100
163 U/mL penicillin, and 100 μg/mL streptomycin (Gibco) at 37 °C in a 5% CO_2/95% air atmosphere.

164 *Expression of ANAP-tagged proteins.* ANAP-tagged proteins were obtained as previously
165 described (Chatterjee et al., 2013; Puljung et al., 2019; Puljung, 2021). Cells were co-
166 transfected with 1 μg of 5-HT_{3A} plasmid with an amber stop codon (TAG) replacing the codon
167 corresponding to amino acid Y234 and downstream mOrange tag, as well as pANAP, which
168 encodes a tRNA with the appropriate anticodon (CUA) to recognize the amber stop codon and a
169 synthetase enzyme capable of charging the tRNA with ANAP. Cells were transfected using
170 TransIT transfection reagent (Mirus; Madison, WI) at a ratio of 3 μL/μg of DNA. Just prior to
171 transfection, the culture medium was replaced with DMEM supplemented with FBS,
172 penicillin/streptomycin, and 20 μM ANAP methyl ester (AsisChem Inc.; Waltham, MA).
173 Experiments were typically performed 2 days post-transfection.

174 *Electrophysiology.* Currents were recorded in the whole-cell patch-clamp configuration. Data
175 were acquired using a Sutter IPA amplifier controlled by SutterPatch software (Sutter
176 Instruments; Novato, CA). Data were digitized at 10 kHz and low-pass filtered at 1 kHz. Patch
177 pipettes were pulled from borosilicate glass (World Precision Instruments 1B150F-4) to a

178 resistance of 8-10 MΩ. The pipette solution contained 140 mM KCl, 1.2 mM $MgCl_2$, 2.6 mM
179 $CaCl_2$, and 10 mM HEPES, pH 7.4 with N-methyl-D-glucamine. The bath solution contained 140
180 mM NaCl, 2.8 mM KCl, 2 mM $MgCl_2$, 1 mM $CaCl_2$, and 10 mM HEPES, pH 7.4 with N-methyl-D-
181 glucamine. Bath solution was exchanged using a MiniStar peristaltic pump (World Precision
182 Instruments). 5-HT was applied in bath solution (supplemented with 5 mM glutathione) using a
183 pressure-driven SmartSquirt Micro-Perfusion System (AutoMate Scientific; Berkeley, CA).

184 *Unroofing HEK cells for imaging.* Cells were unroofed to obtain isolated plasma membranes
185 (Heuser, 2000; Usher et al., 2020a). A small fragment of glass coverslip with adherent HEK293T
186 cells expressing labeled channels was broken off using jeweler's forceps. The fragment was
187 dipped in a solution of 0.1% poly-L-lysine for 3x 10 s. Fragments were blotted (cell-side down)
188 on a clean piece of filter paper (Cytiva Whatman Grade 1; Wilmington, DE), leaving behind
189 adherent plasma membrane fragments.

190 *Microscopy/spectroscopy in living cells/cell fragments.* For experiments, cells were plated in 35
191 mm dishes (Thermo Scientific; Waltham, MA) on glass coverslips (#1 thickness; Chemglass Life
192 Sciences; Vineland, NJ) or on FluoroDishes (World Precision Instruments; Sarasota, FL) a day
193 before transfection. Cells were imaged in the same bath solution used for patch clamp using a
194 Nikon TE2000-U (Melville, NY) or Ti2E microscope equipped with a 60X water-immersion
195 objective (Nikon Plan Apo VC, 1.20 NA). ANAP was excited using a ThorLabs LED source
196 (LED4D067; Newton, NJ) with a center wavelength of 385 nm. For imaging ANAP, the filter set
197 contained a 390/18 nm band-pass filter (MF390-18, ThorLabs), an MD416 dichroic mirror
198 (ThorLabs) and a 470/40 nm band-pass filter (MF479-40, ThorLabs). To obtain spectra, the
199 emission filter was replaced with a 400 nm long-pass filter (FEL0400, ThorLabs). To image the
200 mOrange tag, the same light source was used with a broad LED centered at 565 nm. A 530-30
201 band-pass filter was used for excitation (Chroma; Bellows Falls, VT) with a T550lpxr dichroic
202 mirror (Chroma) and 575/50 band pass emission filter (Chroma).

203 Images and spectra were collected using an IsoPlane81 camera/spectrograph (Teledyne
204 Princeton Instruments; Princeton, NJ) or IsoPlane160/PIXIS 256 camera (Teledyne Princeton
205 Instruments). Image/spectrum acquisition was automated using a Sutter IPA amplifier controlled
206 by SutterPatch software (Sutter Instruments). Exposure times were typically 10 s.
207 Photobleaching artifacts were corrected as previously described (Puljung et al., 2019; Usher et
208 al., 2020a). Briefly, five images were acquired in the absence of 5-HT, the peak intensity of the
209 ANAP spectrum was plotted as a function of exposure time, and the intensity decay was fit with
210 a single exponential. The resulting fit curve was used to correct subsequent exposures. For
211 quenching experiments, 5-HT in bath solution (or bath solution + 5 mM glutathione in unroofed
212 experiments) was applied using a SmartSquirt perfusion system controlled by SutterPatch.
213 Wash times were 10-30 s to ensure that ligand binding reached a steady state. The FluoroDish
214 was perfused with bath solution using a MiniStar peristaltic pump. Solutions were diluted from
215 frozen stocks just prior to the experiment and stored on ice.

216 *Data analysis.* Spectra and chromatograms were analyzed and plotted using custom code
217 written in R version 4.5.0, with plotly, hyperSpec, beepr, ggplot2, gridExtra, and xlsx packages
218 (Wickham, 2016; Auguie, 2017; Dragulescu and Arendt, 2020; Sievert, 2020; Beleites and
219 Sergo, 2024; Bååth, 2024; R Core Team, n.d.). Time-resolved spectroscopic data were
220 analyzed using custom code in Python 3.9.13. Images were analyzed and displayed using Fiji
221 (Schindelin et al., 2012). Additional plots, and curve fits were carried out using JMP 2025 JMP®
222 (version 18.2.2; JMP Statistical Discovery LLC, Cary, NC).

223 To compare concentration-response relationships between cells/membranes, peak
224 fluorescence from bleach-corrected spectra from each cell/membrane were normalized by
225 subtracting the minimum fluorescence at saturating concentrations and dividing by the peak at
226 the lowest applied 5-HT concentration (where no appreciable quenching was evident).
227 Concentration-response data were fit with curve of the form

228 $$\frac{(F-F_{min})}{(F_{max}-F_{min})} = \frac{1}{1+10^{h*((\log EC_{50}-\log[5-HT])}},$$

229 where [5-HT] is the concentration of 5-HT, F is fluorescence, F_{max} is the fluorescence intensity at
230 the lowest [5-HT] concentration (where we observed no appreciable quenching), F_{min} is the
231 fluorescence intensity at the highest [5-HT], and EC_{50} is the concentration that produced half-
232 maximal quenching.

233 *Data presentation and statistics.* For solution spectra, data are displayed as the average of
234 three samples (two for 20 μM ANAP in DMSO). For data from cells and unroofed membranes,
235 all of the individual data points were displayed. Errors are displayed as mean ± SEM. *n* values
236 and fit parameters are included in the figure legends. No power analyses were conducted prior
237 to our experiments to determine the number of repetitions. Protein structures were displayed
238 using ChimeraX developed by the Resource for Biocomputing, Visualization, and Informatics at
239 the University of California, San Francisco with support from National Institutes of Health RO1-
240 GM129325 and the Office of Cyber Infrastructure and Computational Biology, National Institute
241 of Allergy and Infectious Disease (Pettersen et al., 2021). Chemical structures were created and
242 formula masses predicted using ChemDraw (Revvity Signals Software; Waltham, MA).

243 *Materials.* Unless otherwise noted, all chemicals were obtained from Sigma-Aldrich (St. Louis,
244 MO). Restriction enzymes were purchased from ThermoFisher and New England Biolabs, Inc.
245 (Ipswich, MA).

246

247 **Results.**

248 *Steady-state quenching of ANAP by 5-HT and DA in solution.* The fluorophore Prodan,
249 structurally analogous to the side chain of ANAP, is quenched by tryptophan in micelles and
250 when both molecules are incorporated into cytochrome P450 (Pospíšil et al., 2014). Given its
251 similarity to Prodan and its utility as a site-specific protein label, we sought to determine whether
252 ANAP could be quenched by 5-HT, a neurotransmitter derived from tryptophan. We first
253 measured the quenching of ANAP by 5-HT in aqueous solutions. At high concentrations (10
254 mM-50 mM), 5-HT caused a blue shift in ANAP fluorescence (from 499 nm to 487 nm) as well
255 as a 53% reduction in the peak intensity (Fig. S1). The blue shift was likely the result of ANAP's
256 reported environmental sensitivity (Chatterjee et al., 2013). To reduce any solvatochromatic
257 shifts and focus solely on quenching, we measured the spectrum of 20 μM at varying 5-HT
258 concentrations in DMSO. In DMSO, the peak emission wavelength was 451 nm. Thus, this
259 greatly reduced any additional the shift induced by 5-HT binding.

260 In DMSO, 5-HT greatly attenuated the peak ANAP fluorescence in a concentration-dependent
261 manner (Fig. 1B). Quenching was evident at concentrations of 5 mM 5-HT and above. A Stern-
262 Volmer plot of the quenching data was well fit with a straight line (Fig. 1C; K_{sv} = 13.3 M^{-1},
263 intercept = 0.98, R^2 = 0.998). The linear slope and concentration-dependence are both
264 consistent with collisional quenching. At high concentrations, 5-HT absorbs light over the
265 concentration range at which ANAP is excited and emits light (Fig. S2A). Therefore, the
266 absorbance spectrum of each solution was measured and used to correct for the inner-filter
267 effect. Corrected data for 5-HT quenching are shown in Fig. S3A. Whereas there was some
268 deviation from linearity after applying this correction, the resulting Stern-Volmer plot was still
269 well fit with a straight line (Fig. S3B; K_{sv} = 4.31 M^{-1}, intercept = 0.98, R^2 = 0.977). At low 5-HT
270 concentrations, we observed a slight increase in fluorescence rather than quenching,
271 particularly in the corrected data (Fig. S3A). We attribute this change to a residual

solvatochromatic effect, such as the one we observed in water and the one reported by Chatterjee *et al.* which shows an increase in the apparent quantum yield of ANAP accompanying the blue shift in emission (Chatterjee et al., 2013). Consistent with this, we observed a small, reproducible shift the peak wavelength for ANAP emission from 451 nm to 447 nm in the presence of 100 mM 5-HT (Fig. 1B).

In addition to its significant role as a modulatory neurotransmitter, DA is a weak partial agonist of 5-HT_3-type receptors (Lovinger et al., 2000). Therefore, we tested DA's ability to quench ANAP fluorescence in solution. Similar to 5-HT, DA quenched ANAP fluorescence in a concentration-dependent manner (Fig. 1D). The Stern-Volmer plot for DA quenching was linear (Fig. 1E; K_{sv} = 2.70 M^{-1}, intercept = 0.99, R^2 = 0.975). The shallower slope compared to 5-HT implies a less efficient quenching process for DA (Lakowicz, 2006). DA does not absorb light as strongly as 5-HT over the wavelength range at which ANAP absorbs and emits (Fig. S2B). Nevertheless, we corrected for the inner-filter affect using the absorbance spectra measured for each solution (Fig. S3C). The Stern-Volmer plot for corrected data was still linear and produced a fit with similar parameters (Fig. S3D; K_{sv} = 2.71 M^{-1}, intercept = 0.98, R^2 = 0.953). Quenching of ANAP fluorescence by 5-HT and DA is consistent with criterion 1 of 5, suggesting that ANAP can serve as a useful 5-HT detector.

Time-resolved spectroscopies. Excited-state behaviors of ANAP and 5-HT were further interrogated using time-dependent spectroscopies. Time-resolved photoluminescence measures light emitted per unit time over sub-nanosecond time bins, revealing the fluorescent lifetimes of excited species following pulsed laser excitation. TRPL measurements at 480 nm following excitation with a 355 nm pump laser revealed fluorescence lifetimes shorter than the laser pulse full width at half max (FWHM) of the laser pulse but within range of our detector time resolution (400 ps), producing data most accurately fit by a convolution of IRF and a single exponential decay (Fig. S4); no multiexponential signals were observed. Lifetimes were 2.231 ±

297 0.001 ns for 5-HT and 2.776 ± 0.002 ns for ANAP, with the latter exhibiting the expected
298 qualitatively much larger molar absorptivity and emission. The lifetimes were broadly consistent
299 with published values for ANAP (described by two exponential components of 1.3 ns and 3.3 ns)
300 and 5-HT (4 ns) (Nag et al., 2008; Zagotta et al., 2021), which were measured in different
301 solvents. Our TRPL measurements of emission from a mixture of both compounds exhibited the
302 expected individual 5-HT and ANAP signal components but with decreased overall intensity.

303 Transient absorption spectroscopy uses a white-light "probe" to quantify the time-dependent
304 change in UV-visible absorbance of our system following a laser excitation "pump" pulse; TAS
305 can thus measure the dynamics of the short-lived species that exist in solution after ANAP is
306 quenched by 5-HT. TAS measurements required increasing fluorophore and quencher
307 concentrations to reduce fluorescence background; even so, this background overwhelmed the
308 detector and resulted in artifacts for the few nanoseconds at peak irradiance. Following this
309 artifact, a clear product signal appears and persists for several nanoseconds. To address
310 residual electromagnetic interference (EMI; oscillating pattern) remaining in the TAS signal, we
311 again fit with a convolution of the IRF; a single exponential function provided the best fit
312 (superior to second-order-kinetics t^{-1} or biexponential) and indicated that this product peak fully
313 decayed with a lifetime of 3.18 ± 0.08 ns, consistent with a chemically reversible process (Fig.
314 2A). The slight mismatch between the EMI noise phase in the IRF and TAS data is the result of
315 a beating effect stemming from the signal math necessary to produce the TAS data:

316 $$\Delta absorbance(t) = -log_{10}\left(\frac{I_{pumped}(t) - I_{fluorescence}(t)}{I_{unpumped}(t)}\right)$$

317 A negative ΔOD signal (bleach) may also be observed in TAS measurements, resulting from a
318 reduction in concentration of light-absorbing ground-state ANAP. No bleach signal was
319 observed, though this may be attributable to the strong absorbance of the solution itself in the

area around 350 nm where such a bleach would be expected, resulting in poor signal:noise obscuring the bleach. The initial conditions were fully recovered between shots.

Further conclusions can be drawn from comparing this TAS signal to that observed from the separate solutions of ANAP and 5-HT. ANAP shows a permanent increase in absorbance following the pump pulse, indicating an irreversible change following excitation, whereas 5-HT showed no significant TAS signals. If it were the case that ANAP and 5-HT did not interact, summing the signals of separate ANAP and 5-HT solutions should reproduce the signal of the mixture; instead, the summed signal shows a permanent increase in signal in comparison with the ANAP/5-HT mixture's nearly complete recovery (Fig. 2B).

While FRET or Dexter quenching mechanisms would result in the fluorophore/quencher pair being completely returned to their electrically neutral electronic ground states following the quench, the existence of a longer-lived 3.18 ns signal is consistent with the formation of a charge-transfer state that persists in solution after the quench event has occurred (Kandori et al., 1992; Alsam et al., 2015). In conjunction with DFT results (see below), we therefore attribute the observed product signal to an $ANAP^{\bullet-}$ radical anion resulting from reduction of ANAP by 5-HT. As we have demonstrated in earlier work, aromatic radical anions typically show visible absorbances redshifted from those of their neutral parent species due to the additional occupation of π* orbitals (Hill et al., 2018).

Density Functional Theory. Whereas time-resolved measurements revealed a nanosecond-lifetime excited state consistent with charge transfer (CT) as the mechanism behind the quenching of ANAP, DFT calculations provided additional insight into the directionality of the CT process (Fig. 3). Comparison of the energy of a reduced/oxidized pair (e.g., $ANAP^{-}$/$5\text{-}HT^{+}$) to the ground-state combination ($ANAP^{0}$/$5\text{-}HT^{0}$) revealed the relative stability of each and confirmed that for all combinations of fluorophores (L-ANAP methyl ester, Prodan) and

344 quenchers (5-HT, dopamine), the CT state was always significantly less stable (>70 kcal/mol)
345 than the neutral ground state, consistent with the expected behavior of a reversible CT process.
346 DFT results also consistently showed that electron transfer from quencher to fluorophore (i.e.,
347 fluorophore reduction) resulted in a comparatively more stable CT state (73.0–77.1 kcal/mol,
348 versus 93.2–100.5 kcal/mol for fluorophore oxidation), consistent with the expected greater
349 stability of an electron delocalized in a larger π system (Hoffmann and Olofson, 1966). Energies
350 required to access the fluorophore oxidation pathway correspond to <300 nm photons
351 unavailable in our experiments, whereas the energies associated with the quencher oxidation
352 pathway are in the ~400 nm range accessible with excitation sources employed in this work.
353 This further supports electron transfer from quencher to fluorophore as the quenching
354 mechanism.

355 *Measurement of 5-HT binding to intact, functional 5-HT$_{3A}$ receptors.* With the mechanism and
356 dynamics of ANAP quenching by 5-HT established spectroscopically and computationally, we
357 next expressed ANAP near the ligand binding site of 5-HT$_{3A}$ receptors. 5-HT$_{3A}$ is a PLGIC that is
358 activated by direct 5-HT binding to its extracellular domain (Fig. 4A). 5-HT$_{3A}$ forms functional,
359 homomeric receptors in native and heterologous expression systems (Lambert et al., 1989;
360 Maricq et al., 1991). Typical of PLGICs, 5-HT binds in a conserved ligand-binding pocket formed
361 at the interface of adjacent subunits, where it is coordinated by a cage of aromatic amino acids
362 (Fig. 4B). We sought to express 5-HT$_{3A}$ receptors in which one of the aromatic amino acids
363 (Y234) is replaced with ANAP (5-HT$_{3A}$-Y234ANAP). We chose this site because Y234
364 coordinates 5-HT directly and the expected quenching interaction (via charge transfer) should
365 only operate over very short distances (Fig. 4B). Furthermore, as tyrosine is a bulky aromatic
366 amino acid, substitution with ANAP should be relatively conservative.

367 To express 5-HT$_{3A}$-Y234ANAP channels, the gene for mouse 5-HT$_{3A}$ in the pICherryNeo
368 vector was mutated to replace the triplet encoding Y234 with the amber (TAG) stop codon.

369 When expressed alone in HEK293T cells, the resulting plasmid is expected to result in the
370 expression of 5-HT_{3A} prematurely truncated at position 233 in the extracellular region preceding
371 the first transmembrane domain. To obtain full-length, ANAP labeled channels, cells were co-
372 transfected with pANAP, which encodes a tRNA that recognizes the amber stop codon and a
373 synthetase enzyme capable of charging this tRNA with ANAP. ANAP was added to the cell
374 culture media at the time of transfection. When both plasmids and ANAP are present (Fig. 5A),
375 full-length 5-HT_{3A}-Y234ANAP channels can be produced. As an additional control, we inserted
376 an mOrange protein tag in an unstructured cytoplasmic loop downstream of amino acid 234.
377 Thus, orange fluorescence (in addition to ANAP fluorescence) indicates successful
378 incorporation of the label and translation of full-length channels.

379 Figure 5A shows a series of images of HEK293T cells transfected with the plasmid encoding
380 5-HT_{3A}-Y234ANAP. When this plasmid was co-transfected with pANAP and ANAP was included
381 in the culture media, there was obvious fluorescence for both ANAP and mOrange, indicating
382 the presence of full-length, ANAP-labeled channels. When ANAP was omitted from the bathing
383 medium, we typically observed no fluorescence for either ANAP or mOrange, indicating that
384 there was no read-through of the amber stop codon without ANAP present. When ANAP was
385 present, but pANAP was not included in the transfections, again no mOrange fluorescence was
386 observed. The small, diffuse ANAP fluorescence we observed likely represents unincorporated
387 ANAP accumulating inside cells. However, we cannot exclude the possibility that ANAP may be
388 incorporated into other cellular proteins. Regardless, we identified cells for further
389 experimentation based on the presence of both ANAP and mOrange fluorescence.

390 Whereas it is necessary to place ANAP very close to the 5-HT in order to observe any short-
391 range quenching via charge transfer, mutating amino acids so near the ligand binding site runs
392 the risk of altering the receptor's response to 5-HT. Thus, we used whole-cell patch-clamp
393 electrophysiology to verify that 5-HT_{3A}-Y234ANAP receptors were functional and responded to

394 5-HT. Figure 5B shows a typical whole-cell current response to 240 μM 5-HT for an HEK293T
395 cell expressing 5-HT_{3A}-Y234ANAP. Bath application of 5-HT produced a desensitizing current
396 typical of 5-HT_{3A}. We observed an average of 41.2 ± 9.9 pA of current in response to
397 applications of 24 μM 5-HT in5/7 cells that we identified based on mOrange fluorescence. Thus,
398 we can conclude that 5-HT_{3A}-Y234ANAP receptors are present at the plasma membrane and
399 maintain their response to 5-HT, despite alterations to the ligand binding site.

400 To measure 5-HT binding to 5-HT_{3A}-Y234ANAP, we expressed the receptor in HEK293T cells
401 and imaged them using an inverted microscope coupled to a spectrograph. This allowed us to
402 obtain full emission spectra of ANAP-tagged channels in the plasma membrane (Fig. 5C). The
403 ANAP peak was 495 ± 5 nm, close to the value we measured in aqueous solution, suggesting
404 that ANAP at position 234 of 5-HT_{3A} was accessible to bulk water. The secondary peak at ~560
405 nm corresponds to mOrange (emission maximum 562 nm) (Shu et al., 2006). Application of 5-
406 HT gave rise to a concentration-dependent quenching of ANAP fluorescence. The apparent
407 reduction in mOrange fluorescence was due to the overlap in ANAP and mOrange spectra. At
408 saturating concentrations, 5-HT did not quench 100% of the ANAP fluorescence. Quenching at
409 saturating concentrations was variable, with an average of 66% ± 7%. To compare across cells,
410 we subtracted the fluorescence at saturating [5-HT] from each trace and then normalized to the
411 maximum fluorescence at the lowest agonist concentration (Fig. 5D). The resulting
412 concentration-response relationship was well-fit with a modified Hill equation with half-maximal
413 quenching at 594 nM 5-HT and a slope factor of -0.46. The inability of 5-HT to quench 100% of
414 the fluorescence may be a result of the distance between ANAP and 5-HT or the geometry of
415 the binding site. However, it is possible that the unquenched fluorescence signal arose from
416 ANAP-tagged trafficking intermediates in the ER/Golgi that would not be accessible to 5-HT
417 applied extracellularly. Therefore, we repeated the quenching experiment in unroofed plasma
418 membranes obtained by blotting adherent cells with filter paper (Fig. S5). Blotting removes

419 intracellular organelles, thus reducing any background from trafficking intermediates. We
420 observed a similar concentration-response relationship for quenching in unroofed membranes
421 (EC_{50} = 160 nM, slope factor -0.49). We did not, however, obtain 100% quenching in unroofed
422 cells. Therefore, the inability of 5-HT to completely quench likely reflects the geometry of the
423 binding site or photophysics of the ANAP/5-HT interaction, not an inaccessible population of
424 channels.
425

426 **Discussion.**

427 Based on our results, we propose that ANAP can be used to detect 5-HT binding to its
428 receptors. Our assay meets all five criteria set out in the Introduction. By using fluorescence, we
429 measured binding in real-time to intact, functional channels in living cells. Based on our time-
430 resolved fluorescence and transient absorption measurements, we observed a reversible
431 quenching process that recovers with a time constant of 3.2 ns, likely due to back-electron
432 transfer from the reduced fluorophore. This recovery time for the intermolecular process
433 represents an upper bound to back-electron transfer within a ligand binding site and is
434 nonetheless much faster than the expected time course of 5-HT dissociation from the channel.
435 Thus, 5-HT can quench the excited ANAP molecules without any irreversible bleaching of the
436 fluorophore. Charge transfer is very sensitive to distance (requiring collision/contact between
437 the fluorophore and quencher). Therefore, ANAP/5-HT CT allows for detection of binding very
438 near to the site of ANAP incorporation and would not be sensitive to 5-HT bound elsewhere.
439 Replacing Y234 in the 5-HT binding site of 5-HT_{3A} still allowed for binding of 5-HT and channel
440 activation. Thus, with sufficient signal-to-noise ratio, this binding assay is compatible with
441 simultaneous measurements of channel current so that ligand occupancy can be directly
442 correlated with changes in function (i.e. activation, desensitization). Finally, our fluorescence-
443 based assay can be readily scaled for use in a 96 or 384-well format to enable medium/high
444 throughput data acquisition.

445 We used ANAP-tagged 5-HT_{3A} receptors in our assay because, as 5-HT_{3A} is an ion channel,
446 we could record currents to verify that our ANAP-tagged receptors were functional, expressed in
447 the plasma membrane, and able to respond to 5-HT. However, this technique should be easily
448 adapted for use in G-protein-coupled 5-HT receptors and 5-HT transporters. Based on our
449 steady-state measurements, ANAP may also be a promising DA detector when incorporated
450 into receptors. DA is a partial agonist of 5-HT_{3A} and comparing current responses and binding

451 measurements between 5-HT and DA may be a promising way to explore the mechanism of
452 partial agonism in these channels. Furthermore, ANAP can be incorporated into the binding site
453 of DA receptors to help illuminate their biological role.

454 The values we obtained from fits to our 5-HT binding data (EC_{50} 594 nM) were in the range of
455 EC_{50} values obtained from functional measurements of recombinant 5-HT_{3A} activity. The EC_{50}
456 for activation of 5-HT_{3A} in HEK293T cells measured with Ca^{2+} imaging was 348 nM (Dubin et al.,
457 1999). In two-microelectrode studies in *Xenopus* oocytes half-maximal current activation
458 occurred at 3.54 μM (Maricq et al., 1991). The differences in the values we obtained may be the
459 result of mutating the 5-HT binding site. Alternatively, the discrepancy may represent state-
460 dependent 5-HT binding. Based on the time course of the channel currents we measured (Fig.
461 5B) and the duration of our 5-HT applications, we assume that we measured the apparent 5-HT
462 affinity for desensitized receptors. However, one should exercise caution when interpreting EC_{50}
463 values as reflecting any true binding affinity. Even for assays that measure “binding” directly, any
464 values reported reflect not only the binding equilibrium, but any coupled conformational
465 equilibria in the channel complex (Colquhoun, 1998).

466 As presented, our method offers great promise for understanding the relationship between
467 binding of transmitters like 5-HT and DA and receptor activation. However, there are several
468 points of caution worth considering. Our primary difficulty is that, even at saturating
469 concentrations of 5-HT, maximal quenching of 5-HT_{3A}-Y234ANAP was only around 66% and
470 variable. Whereas the signal-to-noise ratio allowed us to generate reproducible binding curves
471 in whole cells and unroofed membranes, more robust and more reproducible quenching at
472 saturating 5-HT concentrations is desirable. Replacement of other aromatic amino acids in the
473 binding site with ANAP may produce better results.

We used long (10-30 s) applications of 5-HT in our experiments and 10 s exposure times for our spectra. On this time scale, 5-HT_{3A}-Y234ANAP receptors were likely in the desensitized state. To capture shorter-lived gating intermediates, faster solution exchange and shorter exposure times will be necessary. The latter will be easier to achieve in preparations with greater signal-to-noise. Alternatively, mutations that reduce sensitization or allosteric modulators that delay it may help explore binding to the open state.

ANAP, with its sensitivity to both 5-HT and DA, shows great promise as a neurotransmitter detector. ANAP is easily inserted co-translationally into any site on a target receptor using amber stop-codon suppression. As ANAP insertion produced functional channels future experiments will allow us to explore the relationship between ligand binding and channel gating for both the full agonist 5-HT and the partial agonist DA. In our previous work, simultaneous measurements of ligand binding and changes in current allowed us to constrain K_{ATP} gating models and derive meaningful parameters regarding true ligand binding affinity and the energetic coupling between binding and activation (Usher et al., 2020b). This approach may also be used to understand how co-assembly of 5-HT_{3A} with other subunits (5-HT_{3B} through 5-HT_{3E}) affects this process as well as how mutations associated with diseases like IBS, drug abuse disorder, and schizophrenia can affect the channel's biophysical properties. Finally, this technique can be readily adapted to study other 5-HT and DA receptors and transporters, offering a real-time window into their structure and activity.

Acknowledgments. This material is based upon work supported by the National Science Foundation under Grant No. CNS-1919554; any opinions, findings, and conclusions or recommendations expressed in this material are those of the authors and do not necessarily represent the views of the National Science Foundation. We wish to thank Robin Kelly, Jim McLaren, and Erin Mostoller for administrative and technical support. We also thank Dr. Jon Ashby and Dr. Lindsey Hanson for critical feedback. This work was supported financially by the Beckman Scholars program from the Arnold and Mabel Beckman Foundation, the Trinity College Interdisciplinary Science Program, and startup funds from Trinity College. We thank St. Lawrence University for access the Ada high-performance computer, a Warewulf Community Support Cluster system.

505 **Figure Legends.**

506 Figure 1. Quenching of ANAP by 5-HT and DA in solution. A. Molecular structures of ANAP, 5-
507 HT, and DA. B. Emission spectra (excitation 370 nm) of 20 μM ANAP in DMSO in the absence
508 and presence of 5-HT. C. Stern-Volmer plot for 5-HT quenching of ANAP. The relationship was
509 fit with a straight line with an intercept of 0.98 and a slope (K_{sv}) of 13.3 M^{-1} (R^2 = 0.998). D.
510 Emission spectra (excitation 370 nm) of 20 μM ANAP in DMSO in the absence and presence of
511 DA. E. Stern-Volmer plot for DA quenching of ANAP. The relationship was fit with a straight line
512 with an intercept of 0.99 and a slope (K_{sv}) of 2.70 M^{-1} (R^2 = 0.975).

513

514 Figure 2. Transient absorption of 1.0 mM L-ANAP methyl ester and 10 mM 5-HT solution at 440
515 nm following excitation at 355 nm, showing (a) the appearance and recovery of a short-lived
516 product peak attributed to reduced ANAP; convolution fit lifetime of the resulting recovery was
517 3.18 ± 0.08 ns. (b) ANAP & 5-HT mixture (black; with 21-point second-order Savitzky-Golay
518 smoothing) exhibits complete recovery (green dashed line) while with a sum of signals from the
519 two separate solutions (violet) shows a long-lived transient signal (violet dashed line).

520

521 Figure 3. DFT-calculated redox ΔG values for electron transfer reactions of L-ANAP methyl
522 ester or Prodan with dopamine or 5-HT (ωB97XD density functional and aug-cc-pVDZ basis),
523 showing that fluorophore reduction/quencher oxidation is consistently more thermodynamically
524 stable. Structures shown above are those of the most redox-stable radical species.

525

526 Figure 4. Structure of 5-$HT_{3A^{\cdot}}$ A. Cryo-electron microscopy structure of 5-HT_{3A}. Subunits are
527 individually colored. 5-HT is shown as a gray, space-filling model. B. One (of five) 5-HT binding

528 sites in 5-HT_{3A} highlighting nearby aromatic residues. Structural models are from Basak *et al.*
529 ((Basak et al., 2018), PDB accession number 6DG8).

530

531 Figure 5. 5-HT binding to 5-HT_{3A}-Y234ANAP. A. Brightfield and fluorescence micrographs
532 showing cells co-expressing the 5-HT_{3A}-Y234TAG plasmid and pANAP and cultured in the
533 presence (left) and absence (middle) of ANAP. The right panel shows cells expressing the 5-
534 HT_{3A}-Y234TAG plasmid without pANAP and cultured in the presence of ANAP. B.
535 Representative whole-cell currents in response to bath application of 240 μM 5-HT for a cell
536 expressing 5-HT_{3A}-Y234ANAP. C. Fluorescence emission spectra acquired from a cell
537 expressing 5-HT_{3A}-Y234ANAP in the presence of increasing concentrations of 5-HT. D. Data
538 from 7 cells expressing 5-HT_{3A}-Y234ANAP showing the normalized quenching by 5-HT. The
539 data were fit to a modified Hill equation (see Materials and Methods) with a slope of -0.46 and
540 EC_{50} value of 594 nM. The shaded area shows the 95% confidence interval for the fit.

541

542 Supplemental Figure S1. Quenching of ANAP by 5-HT in water. Emission spectra (excitation
543 370 nm) of 20 μM ANAP in water in the absence and presence of 5-HT.

544

545 Supplemental Figure S2. Absorbance spectra of ANAP with 5-HT or DA in DMSO. A.
546 Absorbance spectra for solutions of 20 μM ANAP plus the indicated amount of 5-HT in DMSO.
547 B. Absorbance spectra for solutions of 20 μM ANAP plus the indicated amount of DA in DMSO.
548 The smooth lines are the spectra after local kernel smoothing was applied. Each spectrum is the
549 average of three samples.

550 Supplemental Figure S3. Inner-filter-corrected spectra. A. Emission spectra (excitation 370 nm)
551 of 20 μM ANAP in DMSO in the absence and presence of 5-HT, corrected for the inner-filter
552 effect (see Materials and Methods). B. Stern-Volmer plot for 5-HT quenching of ANAP. Data
553 were corrected for the inner-filter effect. The relationship was fit with a straight line with an
554 intercept of 0.98 and a slope (K_{sv}) of 4.31 M^{-1} (R^2 = 0.977). C. Emission spectra (excitation 370
555 nm) of 20 μM ANAP in DMSO in the absence and presence of DA, corrected for the inner-filter
556 effect. D. Stern-Volmer plot for DA quenching of ANAP. Data were corrected for the inner-filter
557 effect. The relationship was fit with a straight line with an intercept of 0.98 and a slope (K_{sv}) of
558 2.71 M^{-1} (R^2 = 0.953).

559

560 Supplemental Figure S4. Time-resolved photoluminescence at 470 nm following excitation at
561 355 nm of 10 mM 5-HT (top) and 100 nM L-ANAP methyl ester (bottom) with fits (red) calculated
562 from the convolution of the instrument response function (gray) and exponential decay, resulting
563 in fluorescence lifetimes of 2.231 ± 0.001 ns and 2.776 ± 0.002 ns, respectively.

564

565 Supplemental Figure S5. 5-HT binding to 5-HT_{3A}-Y234ANAP in unroofed plasma membranes.
566 Data from 3 unroofed plasma membranes from cells expressing 5-HT_{3A}-Y234ANAP showing the
567 normalized quenching by 5-HT. The data were fit to a modified Hill equation (see Materials and
568 Methods) with a slope of -0.49 and EC_{50} value of 160 nM. The shaded area shows the 95%
569 confidence interval for the fit.
570

571 **References**

572 Alsam, A. A., Aly, S. M., Usman, A., Parida, M. R., Del Gobbo, S., Alarousu, E., et al. (2015).
573 Bimolecular Excited-State Electron Transfer with Surprisingly Long-Lived Radical Ions. *J.*
574 *Phys. Chem. C* 119, 21896–21903. doi: 10.1021/acs.jpcc.5b06636

575 Auguie, B. (2017). _gridExtra: Miscellaneous Functions for "Grid" Graphics_. R package
576 version 2.3.

577 Bååth, R. (2024). _beepr: Easily Play Notification Sounds on any Platform_. R package
578 version 2.0,. Available at: https://CRAN.R-project.org/package=beepr

579 Basak, S., Gicheru, Y., Rao, S., Sansom, M. S. P., and Chakrapani, S. (2018). Cryo-EM reveals
580 two distinct serotonin-bound conformations of full-length 5-HT3A receptor. *Nature* 563,
581 270–274. doi: 10.1038/s41586-018-0660-7

582 Beleites, C., and Sergo, V. (2024). hyperSpec: a package to handle hyperspectral data sets in
583 R', R package version 0.100.2. Available at: https://github.com/r-hyperspec/hyperSpec

584 Bursch, M., Mewes, J., Hansen, A., and Grimme, S. (2022). Best-Practice DFT Protocols for
585 Basic Molecular Computational Chemistry**. *Angew Chem Int Ed* 61, e202205735. doi:
586 10.1002/anie.202205735

587 Chai, J.-D., and Head-Gordon, M. (2008). Long-range corrected hybrid density functionals with
588 damped atom–atom dispersion corrections. *Phys. Chem. Chem. Phys.* 10, 6615. doi:
589 10.1039/b810189b

590 Chatterjee, A., Guo, J., Lee, H. S., and Schultz, P. G. (2013). A Genetically Encoded
591 Fluorescent Probe in Mammalian Cells. *J. Am. Chem. Soc.* 135, 12540–12543. doi:
592 10.1021/ja4059553

593 Colquhoun, D. (1998). Binding, gating, affinity and efficacy: the interpretation of structure-activity
594 relationships for agonists and of the effects of mutating receptors. *Br J Pharmacol* 125,
595 924–947. doi: 10.1038/sj.bjp.0702164

596 Dragulescu, A., and Arendt, C. (2020). _xlsx: Read, Write, Format Excel 2007 and Excel
597 97/2000/XP/2003 Files_. R package version 0.6.5.

598 Dubin, A. E., Huvar, R., D'Andrea, M. R., Pyati, J., Zhu, J. Y., Joy, K. C., et al. (1999). The
599 pharmacological and functional characteristics of the serotonin 5-HT(3A) receptor are
600 specifically modified by a 5-HT(3B) receptor subunit. *J Biol Chem* 274, 30799–30810.
601 doi: 10.1074/jbc.274.43.30799

602 Ellenbroek, B. A., and Prinssen, E. P. M. (2015). Can 5-HT3 antagonists contribute toward the
603 treatment of schizophrenia? *Behav Pharmacol* 26, 33–44. doi:
604 10.1097/FBP.0000000000000102

605 Engleman, E. A., Rodd, Z. A., Bell, R. L., and Murphy, J. M. (2008). The role of 5-HT3 receptors
606 in drug abuse and as a target for pharmacotherapy. *CNS Neurol Disord Drug Targets* 7,
607 454–467. doi: 10.2174/187152708786927886

Gibbs, E., and Chakrapani, S. (2021). “Structure, Function and Physiology of 5-Hydroxytryptamine Receptors Subtype 3,” in *Macromolecular Protein Complexes III: Structure and Function*, eds. J. R. Harris and J. Marles-Wright (Cham: Springer International Publishing), 373–408. doi: 10.1007/978-3-030-58971-4_11

Hensler, J. G. (2012). “Serotonin,” in *Basic Neurochemistry*, eds. S. T. Brady, G. J. Siegel, R. W. Albers, and D. L. Price (Academic Press).

Heuser, J. (2000). The Production of ‘Cell Cortices’ for Light and Electron Microscopy. *Traffic* 1, 545–552. doi: 10.1034/j.1600-0854.2000.010704.x

Hill, A. D., Katsoukis, G., and Frei, H. (2018). Photoinduced Electron Transfer from ZrOCo Binuclear Light Absorber to Pyridine Elucidated by Transient Optical and Infrared Spectroscopy. *J. Phys. Chem. C* 122, 20176–20185. doi: 10.1021/acs.jpcc.8b06435

Hoffmann, R., and Olofson, R. A. (1966). The Dependence of Conformational and Isomer Stability on the Number of Electrons in Extended π Systems. *J. Am. Chem. Soc.* 88, 943–946. doi: 10.1021/ja00957a015

Kandel, E. R., Koester, J. D., Mack, S. H., and Siegelbaum, S. A. eds. (2021). *Principles of neural science*., Sixth edition. New York, N.Y: McGraw-Hill Education LLC.

Kandori, H., Kemnitz, K., and Yoshihara, K. (1992). Subpicosecond transient absorption study of intermolecular electron transfer between solute and electron-donating solvents. *J. Phys. Chem.* 96, 8042–8048. doi: 10.1021/j100199a039

Kawate, T., and Gouaux, E. (2006). Fluorescence-detection size-exclusion chromatography for precrystallization screening of integral membrane proteins. *Structure* 14, 673–681. doi: 10.1016/j.str.2006.01.013

Kolber, Z. S., and Barkley, M. D. (1986). Comparison of approaches to the instrumental response function in fluorescence decay measurements. *Analytical Biochemistry* 152, 6–21. doi: 10.1016/0003-2697(86)90111-9

Kremers, G.-J., Hazelwood, K. L., Murphy, C. S., Davidson, M. W., and Piston, D. W. (2009). Photoconversion in orange and red fluorescent proteins. *Nat Methods* 6, 355–358. doi: 10.1038/nmeth.1319

Lakowicz, J. R. (2006). *Principles of fluorescence spectroscopy*., 3rd ed. New York: Springer.

Lambert, J. J., Peters, J. A., Hales, T. G., and Dempster, J. (1989). The properties of 5-HT3 receptors in clonal cell lines studied by patch-clamp techniques. *Br J Pharmacol* 97, 27–40. doi: 10.1111/j.1476-5381.1989.tb11920.x

Lovinger, D. M., Sung, K. W., and Zhou, Q. (2000). Ethanol and trichloroethanol alter gating of 5-HT3 receptor-channels in NCB-20 neuroblastoma cells. *Neuropharmacology* 39, 561–570. doi: 10.1016/s0028-3908(99)00164-1

Maricq, A. V., Peterson, A. S., Brake, A. J., Myers, R. M., and Julius, D. (1991). Primary structure and functional expression of the 5HT3 receptor, a serotonin-gated ion channel. *Science* 254, 432–437. doi: 10.1126/science.1718042

Nag, S., Balaji, J., Madhu, P. K., and Maiti, S. (2008). Intermolecular association provides specific optical and NMR signatures for serotonin at intravesicular concentrations. *Biophys J* 94, 4145–4153. doi: 10.1529/biophysj.107.121384

Ossipov, M. H., Dussor, G. O., and Porreca, F. (2010). Central modulation of pain. *J Clin Invest* 120, 3779–3787. doi: 10.1172/JCI43766

Pettersen, E. F., Goddard, T. D., Huang, C. C., Meng, E. C., Couch, G. S., Croll, T. I., et al. (2021). UCSF ChimeraX: Structure visualization for researchers, educators, and developers. *Protein Sci* 30, 70–82. doi: 10.1002/pro.3943

Pospíšil, P., Luxem, K. E., Ener, M., Sýkora, J., Kocábová, J., Gray, H. B., et al. (2014). Fluorescence quenching of (dimethylamino)naphthalene dyes Badan and Prodan by tryptophan in cytochromes P450 and micelles. *J Phys Chem B* 118, 10085–10091. doi: 10.1021/jp504625d

Puljung, M. C. (2021). “ANAP: A versatile, fluorescent probe of ion channel gating and regulation,” in *Methods in Enzymology*, (Elsevier), 49–84. doi: 10.1016/bs.mie.2021.01.048

Puljung, M., Vedovato, N., Usher, S., and Ashcroft, F. (2019). Activation mechanism of ATP-sensitive K+ channels explored with real-time nucleotide binding. *eLife* 8, e41103. doi: 10.7554/eLife.41103

R Core Team (n.d.). _R: A Language and Environment for Statistical Computing_. Available at: https://www.R-project.org/

Schindelin, J., Arganda-Carreras, I., Frise, E., Kaynig, V., Longair, M., Pietzsch, T., et al. (2012). Fiji: an open-source platform for biological-image analysis. *Nat Methods* 9, 676–682. doi: 10.1038/nmeth.2019

Shao, Y., Gan, Z., Epifanovsky, E., Gilbert, A. T. B., Wormit, M., Kussmann, J., et al. (2015). Advances in molecular quantum chemistry contained in the Q-Chem 4 program package. *Molecular Physics* 113, 184–215. doi: 10.1080/00268976.2014.952696

Shu, X., Shaner, N. C., Yarbrough, C. A., Tsien, R. Y., and Remington, S. J. (2006). Novel chromophores and buried charges control color in mFruits. *Biochemistry* 45, 9639–9647. doi: 10.1021/bi060773l

Sievert, C. (2020). Interactive Web-Based Data Visualization with R, plotly, and shiny.

Tartakoff, S. S., Enders, A. A., Zhang, W., and Hill, A. D. (2021). Spectroscopic and computational evidence for the concerted mechanism of the Wagner-Jauregg reaction. *J of Physical Organic Chem* 34, e4140. doi: 10.1002/poc.4140

Usher, S. G., Ashcroft, F. M., and Puljung, M. C. (2020a). Measuring Nucleotide Binding to Intact, Functional Membrane Proteins in Real Time. *Journal of Visualized Experiments* epub ahead of print.

682 Usher, S. G., Ashcroft, F. M., and Puljung, M. C. (2020b). Nucleotide inhibition of the pancreatic
683 ATP-sensitive K+ channel explored with patch-clamp fluorometry. *eLife* 9, e52775. doi:
684 10.7554/eLife.52775

685 Vahora, I. S., Tsouklidis, N., Kumar, R., Soni, R., and Khan, S. (2020). How Serotonin Level
686 Fluctuation Affects the Effectiveness of Treatment in Irritable Bowel Syndrome. *Cureus*
687 12, e9871. doi: 10.7759/cureus.9871

688 Wickham, H. (2016). ggplot2: Elegant Graphics for Data Analysis.

689 Zagotta, W. N., Sim, B. S., Nhim, A. K., Raza, M. M., Evans, E. G., Venkatesh, Y., et al. (2021).
690 An improved fluorescent noncanonical amino acid for measuring conformational
691 distributions using time-resolved transition metal ion FRET. *Elife* 10, e70236. doi:
692 10.7554/eLife.70236

693

Figure 1

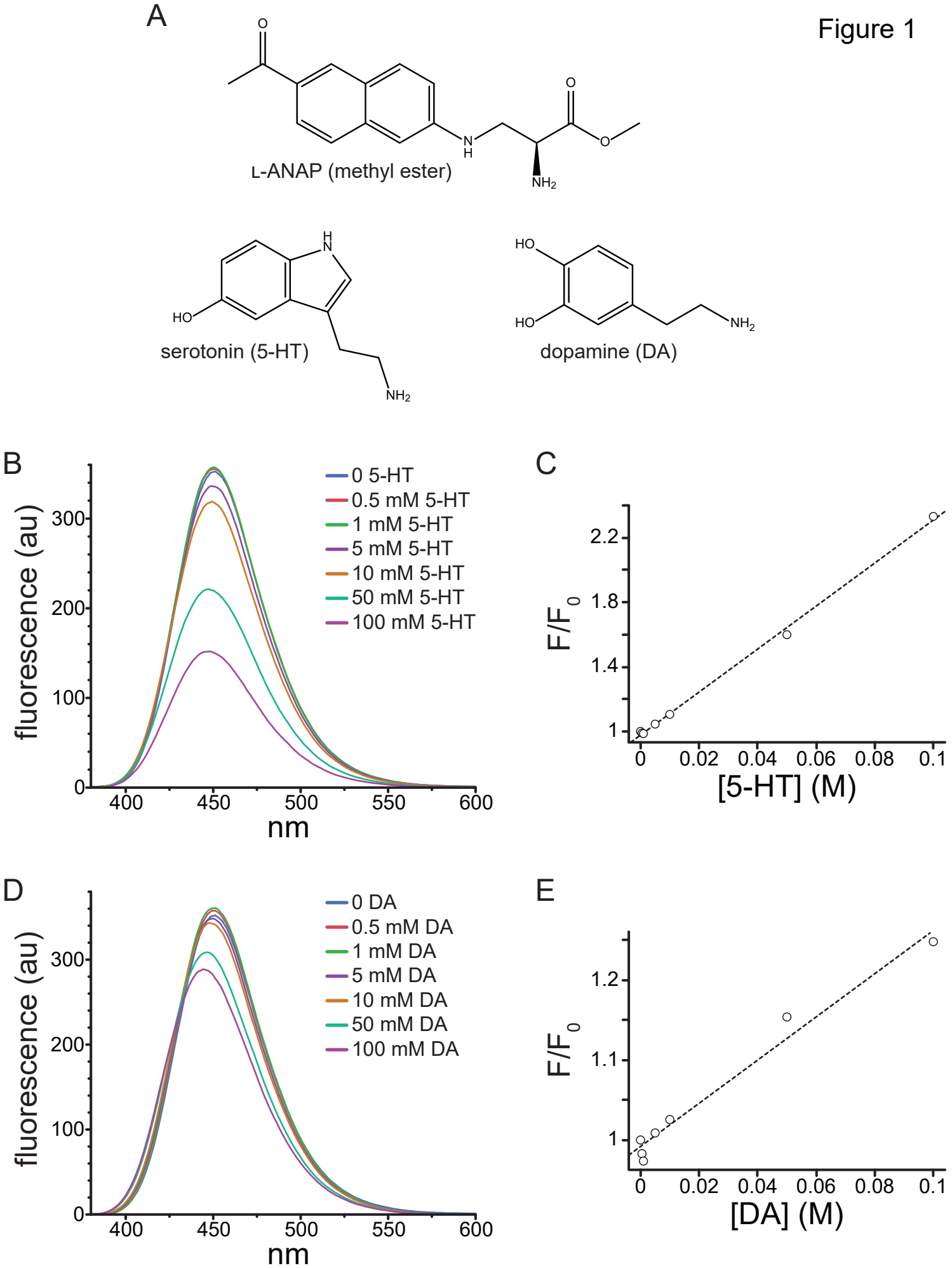
A
L-ANAP (methyl ester)
serotonin (5-HT)
dopamine (DA)
B
fluorescence (au)
nm
0 5-HT
0.5 mM 5-HT
1 mM 5-HT
5 mM 5-HT
10 mM 5-HT
50 mM 5-HT
100 mM 5-HT
C
F/F0
[5-HT] (M)
D
fluorescence (au)
nm
0 DA
0.5 mM DA
1 mM DA
5 mM DA
10 mM DA
50 mM DA
100 mM DA
E
F/F0
[DA] (M)

Figure 2

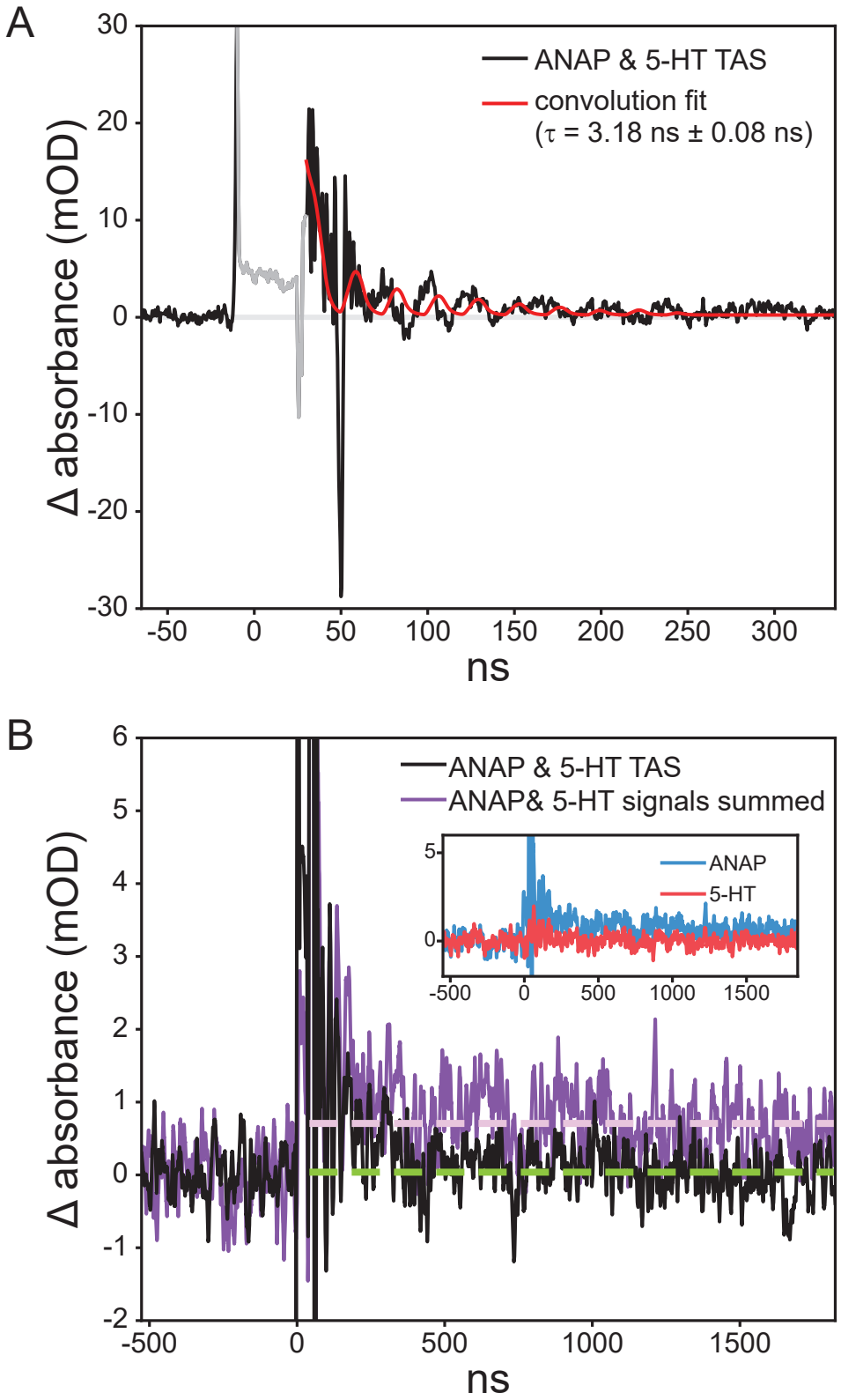
A
ANAP & 5-HT TAS
convolution fit
(τ = 3.18 ns ± 0.08 ns)
Δ absorbance (mOD)
ns
B
ANAP & 5-HT TAS
ANAP& 5-HT signals summed
ANAP
5-HT
Δ absorbance (mOD)
ns

Figure 3

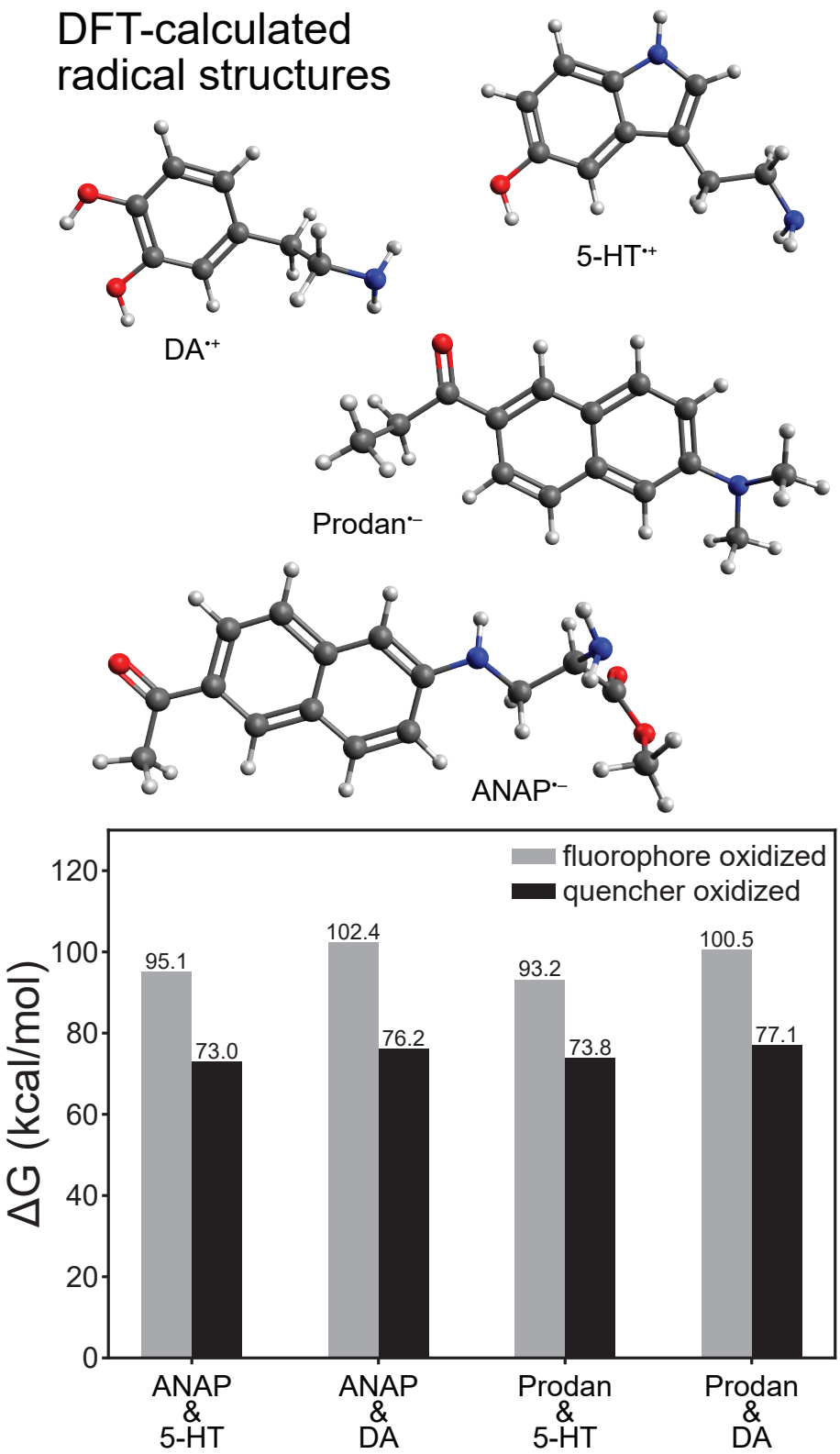
DFT-calculated radical structures
5-HT•+
DA•+
Prodan•−
ANAP•−
fluorophore oxidized
quencher oxidized
ΔG (kcal/mol)
0
20
40
60
80
100
120
95.1
73.0
102.4
76.2
93.2
73.8
100.5
77.1
ANAP & 5-HT
ANAP & DA
Prodan & 5-HT
Prodan & DA

Figure 4

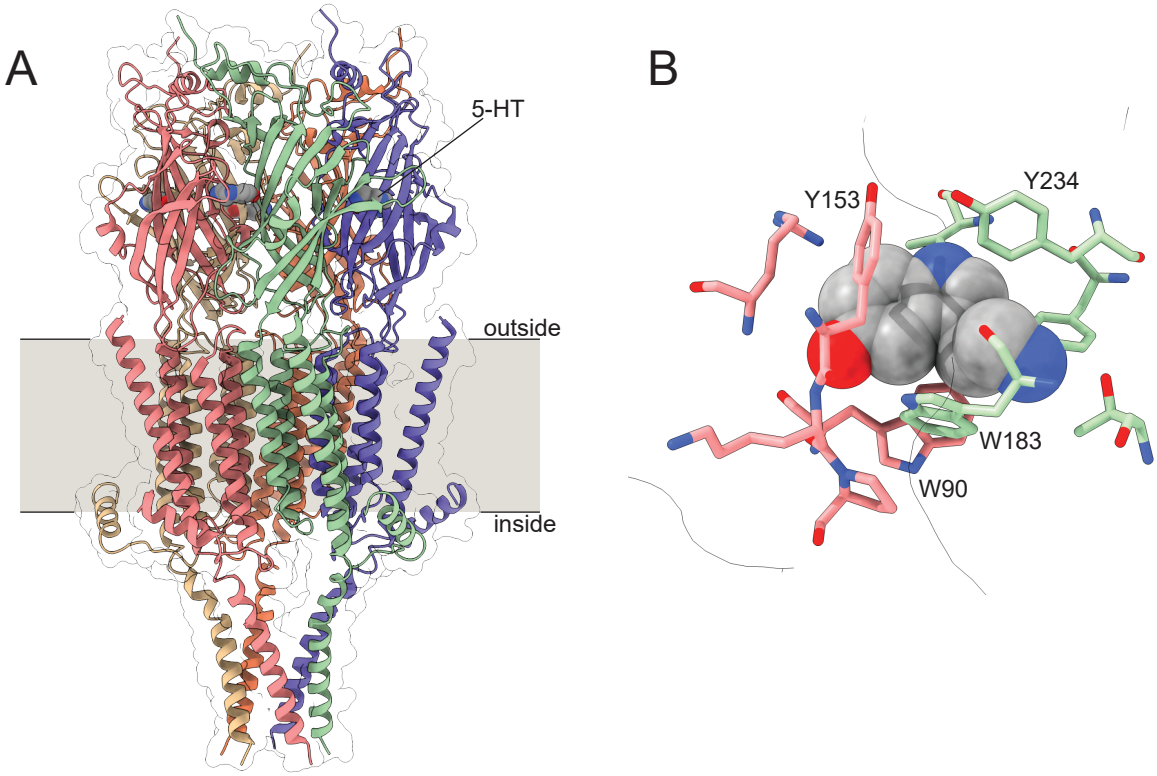

Figure 5

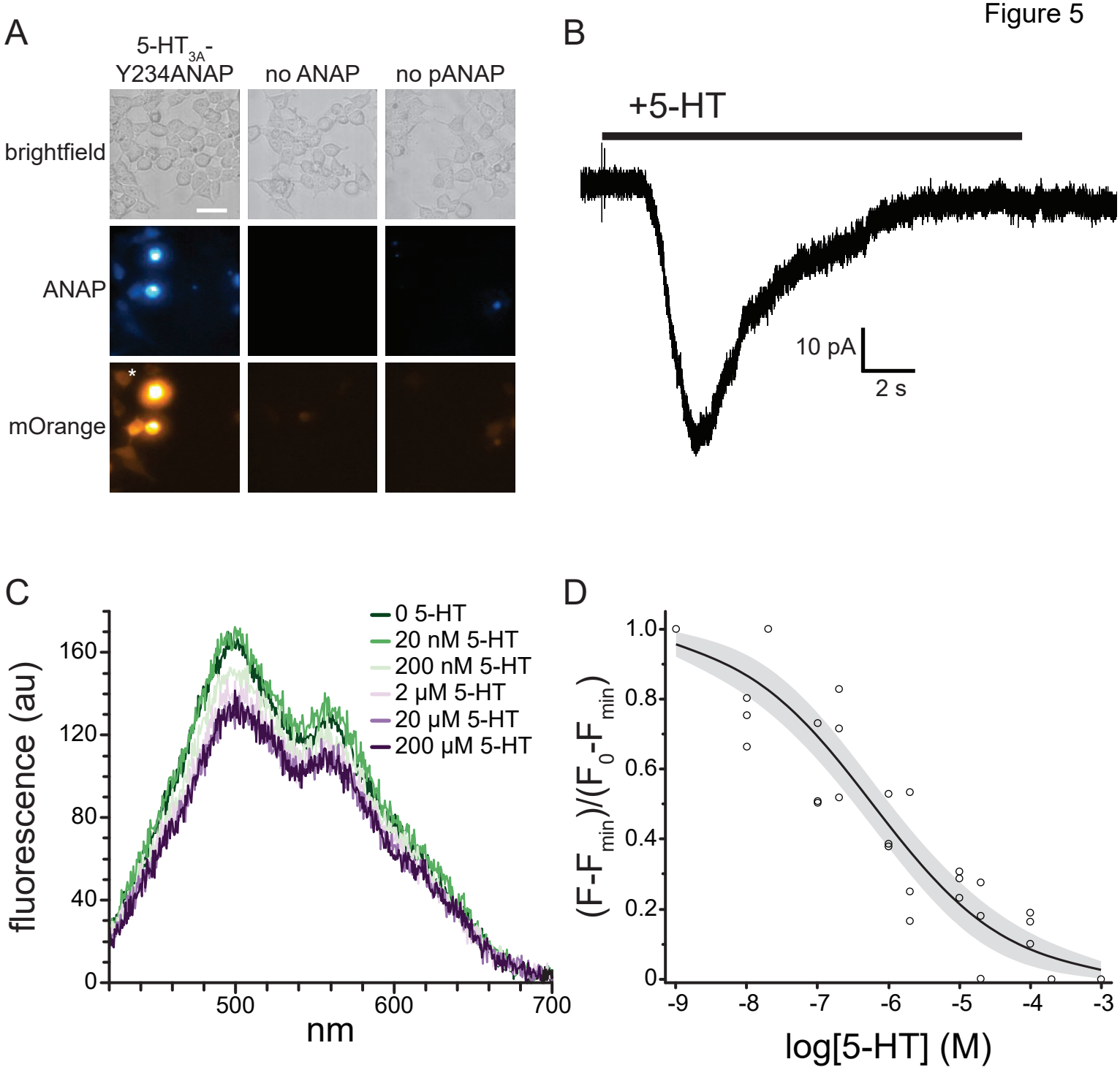
A
5-HT3A-Y234ANAP
no ANAP
no pANAP
brightfield
ANAP
mOrange
*
B
+5-HT
10 pA
2 s
C
0 5-HT
20 nM 5-HT
200 nM 5-HT
2 μM 5-HT
20 μM 5-HT
200 μM 5-HT
fluorescence (au)
nm
D
(F-Fmin)/(F0-Fmin)
log[5-HT] (M)

Figure S1

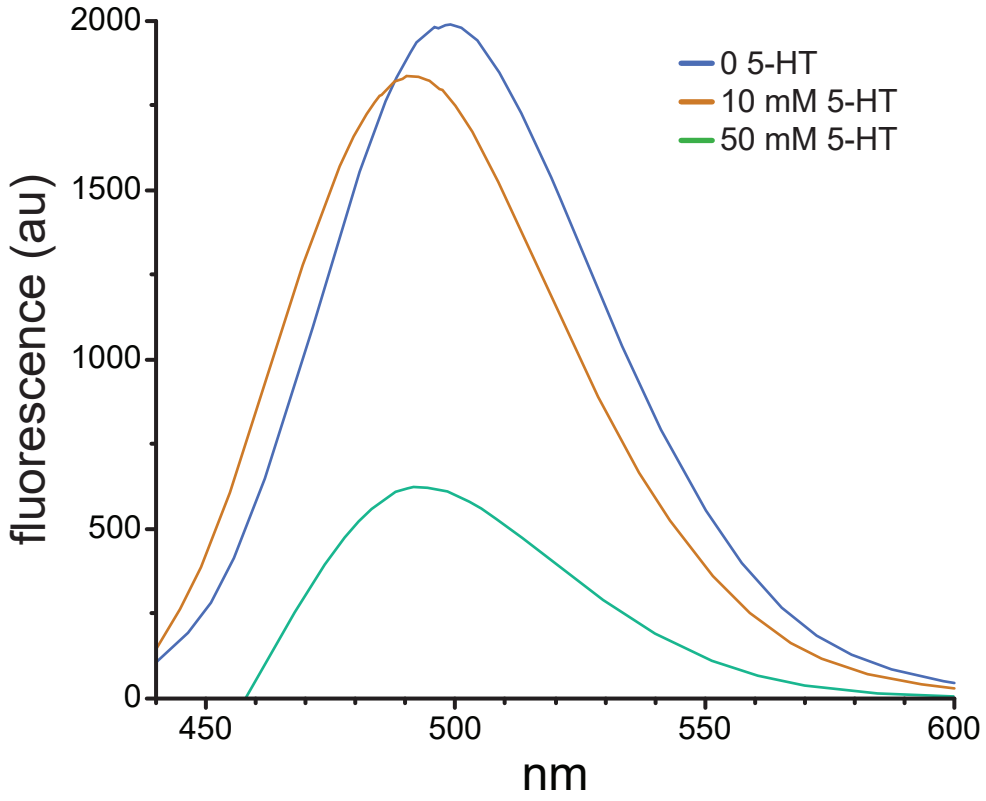
2000
1500
1000
500
0
fluorescence (au)
450
500
550
600
nm
0 5-HT
10 mM 5-HT
50 mM 5-HT

Figure S2

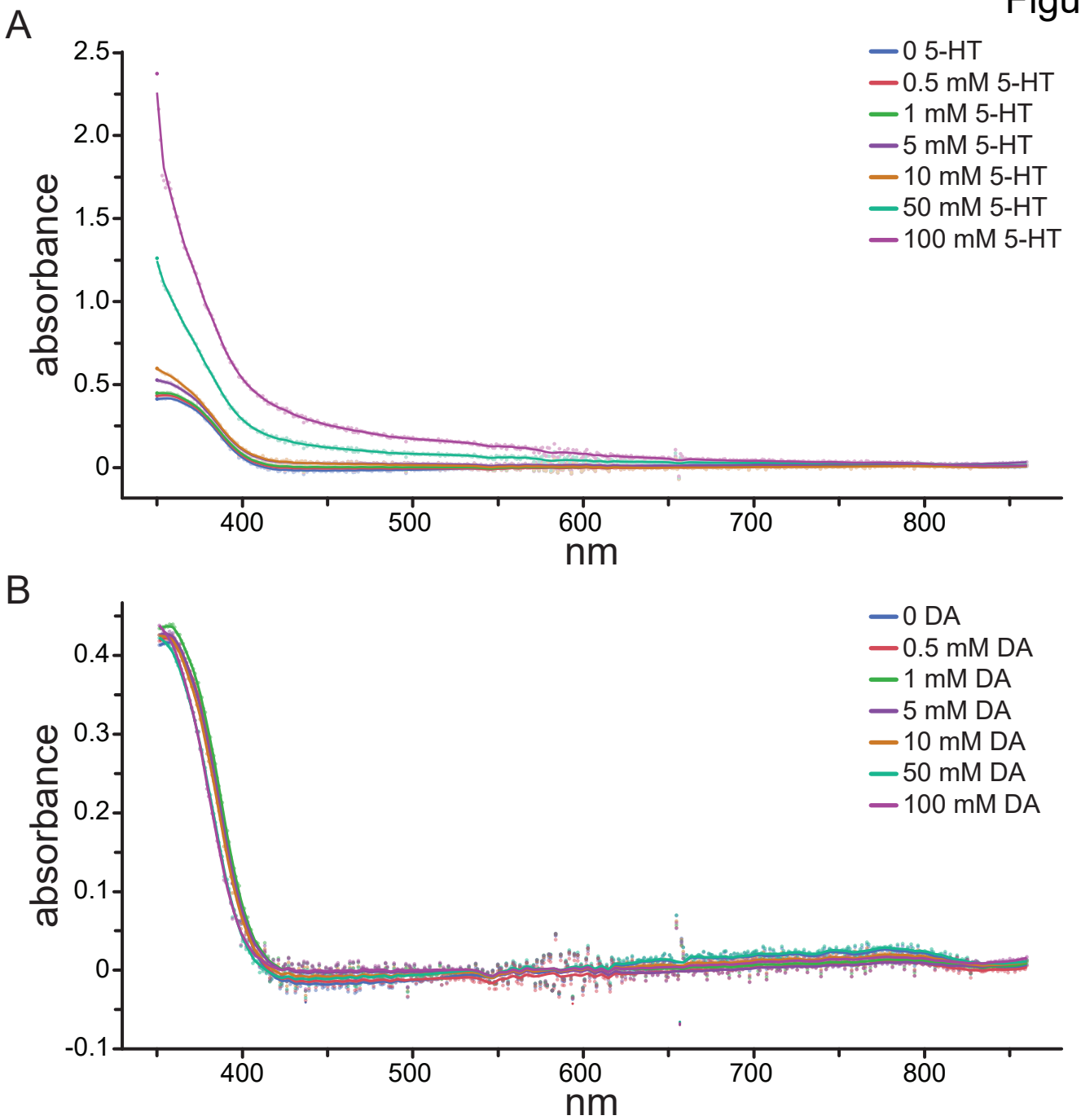
A
absorbance
2.5
2.0
1.5
1.0
0.5
0
400
500
600
700
800
nm
0 5-HT
0.5 mM 5-HT
1 mM 5-HT
5 mM 5-HT
10 mM 5-HT
50 mM 5-HT
100 mM 5-HT
B
absorbance
0.4
0.3
0.2
0.1
0
-0.1
400
500
600
700
800
nm
0 DA
0.5 mM DA
1 mM DA
5 mM DA
10 mM DA
50 mM DA
100 mM DA

Figure S3

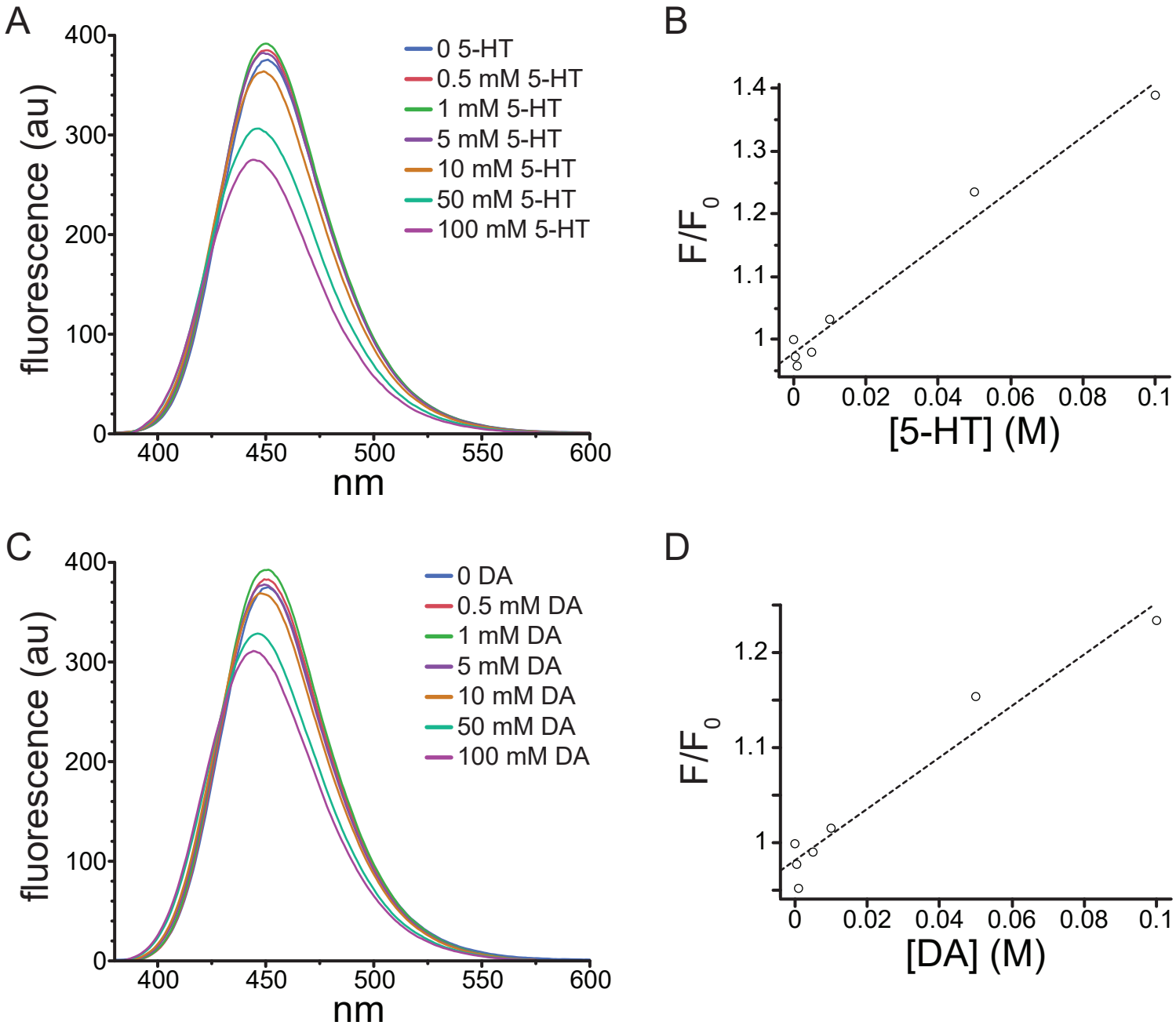
A
fluorescence (au)
nm
0 5-HT
0.5 mM 5-HT
1 mM 5-HT
5 mM 5-HT
10 mM 5-HT
50 mM 5-HT
100 mM 5-HT
B
F/F0
[5-HT] (M)
C
fluorescence (au)
nm
0 DA
0.5 mM DA
1 mM DA
5 mM DA
10 mM DA
50 mM DA
100 mM DA
D
F/F0
[DA] (M)

Figure S4

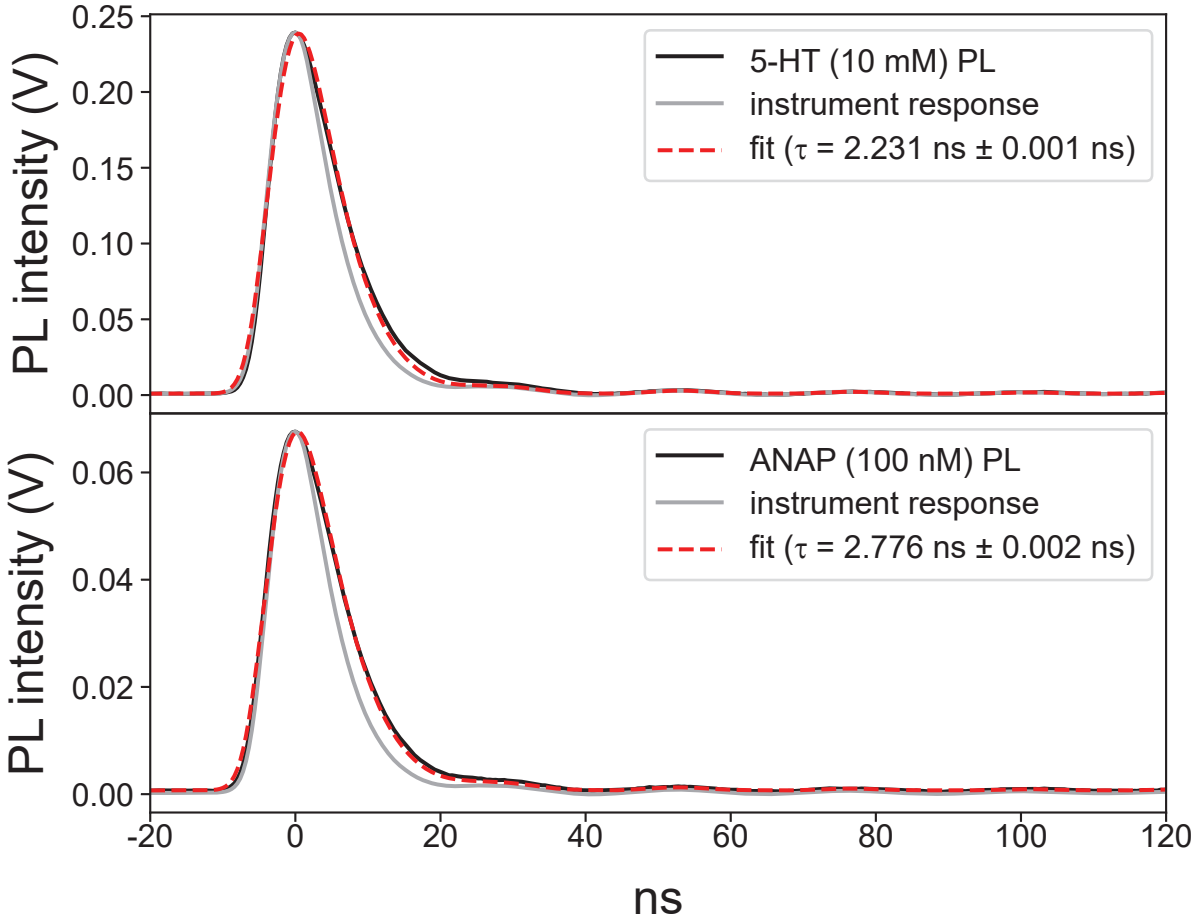
0.25
0.20
0.15
0.10
0.05
0.00
PL intensity (V)
5-HT (10 mM) PL
instrument response
fit (τ = 2.231 ns ± 0.001 ns)
0.06
0.04
0.02
0.00
PL intensity (V)
ANAP (100 nM) PL
instrument response
fit (τ = 2.776 ns ± 0.002 ns)
-20
0
20
40
60
80
100
120
ns
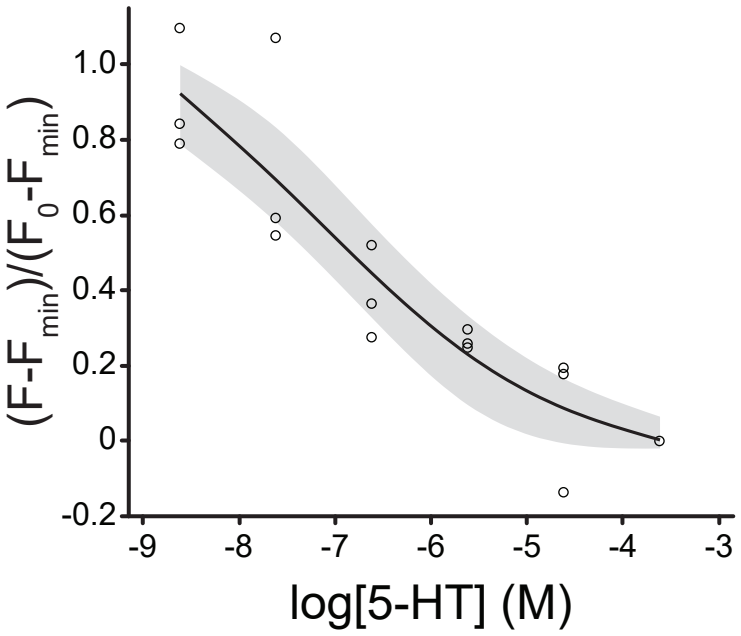
Figure S5